Enhancement of Microwave Imaging Using a Metamaterial Lens

Saptarshi Mukherjee, *Student Member, IEEE*, Zhiyi Su, *Member, IEEE*, Lalita Udpa, *Fellow, IEEE*, Satish Udpa, *Fellow, IEEE*, and Antonello Tamburrino, *Senior Member, IEEE*

***Abstract*— Microwave far-field imaging techniques are well suited to image source, scatterers, and anomalies in dielectric or composite materials. However, the diffraction limits restrict the resolution of far-field imaging. This contribution focuses on the feasibility of designing a metamaterial lens based sensor for enhancing the resolution of microwave far-field imaging. Metamaterials have been increasingly used in the past few decades for the designing of novel microwave circuits and sensor systems. The unique properties of metamterials offer several advantages, such as sub-wavelength nature, compact design, and super-resolution, which is not found in the conventional materials. The feasibility of enhancing imaging resolution using a metamaterial lens along with time reversal processing of far-field microwave data is studied in this paper. Specifically, the super-resolution capability of the lens for detection of sub wavelength defects inside the composite materials is presented.**

***Index Terms*— Metamaterials, microwave imaging, time reversal, NDE, composites.**

I. Introduction

COMPOSITES are being increasingly used in several industries to replace metals, fully or partially due to their unique properties such as high strength, durability and lightweight [1]. They also offer flexibility and strategic tailoring of their mechanical properties. Defects such as disbonds, voids, delaminations may be formed during the manufacturing as well as during service [2]. These defects affect the overall structural strength, performance and integrity and in the long run may lead to catastrophic failure [3]. Thus, there is a need for a reliable nondestructive evaluation (NDE) sensor system that can be utilized to rapidly inspect large areas of composites, and accurately detect potential anomalies [4].

Currently ultrasonics, eddy current, X-ray, infrared thermography and optical imaging are some of the most widely investigated industrial NDE techniques [5], [6]. This paper presents a microwave NDE system for lowloss and lossless dielectric materials [7]. Since electromagnetic waves can penetrate such materials, the scattered fields can be utilized to evaluate the structural integrity of such materials. Some of the recent applications of Microwave NDE are corrosion detection in painted aluminum and steel substrates, flaw detection in Sprayed on Foam Insulation (SOFI) of space shuttles, disbond detection in CFRP strengthened cement based structures [8].

Microwave far field imaging techniques are particularly suited to image source, scatterers and anomalies in dielectric materials [9]. Microwave time reversal is a source focusing method which can be utilized to image defects that act as secondary sources in composite materials [10]. Electromagnetic field components diverging out from a point source can be reversed in time and back-propagated in a numerical model to focus back at the original source location [11]. Introduced by Mathias Fink in 1992 for lithotripsy applications [12], TR was extended to electromagnetic waves by Lerosey *et al.* [13]. Electromagnetic TR is now used widely in radar detection, breast tumor imaging and wireless charging applications [14], [15]. Some of the advantages of using TR over conventional tomographic imaging include its ease of implementation, non-iterative, quasi real-time nature, super-resolution and selective focusing capabilities [16]. Previous far field TR simulation and experimental studies have demonstrated diffraction limited imaging resolution [17]. Objects smaller than the operating wavelength are not detectable in the far field microwave data. While near field imaging techniques provide much higher resolution, the scanning time for large areas can be very high [18]. This paper proposes the use of metamaterials, which can provide higher resolution using far field microwave measurements. Recent work has demonstrated the application of utilizing a metamaterial lens to increase the sensitivity of microwave NDE techniques for detecting subwavelength size defects, in isotropic dielectric materials [19], [20].

Prior experimental results have demonstrated the ability of a metamaterial lens with a relative refractive index of -1, to form images that overcome diffraction limits [21]. This research proposes the inclusion of a metamaterial lens in conjunction with a microwave sensor system in a far field microwave setup, coupled with the TR algorithm for enhanced resolution of imaging. Fig. 1 shows an overview of a far field microwave sensor system for imaging applications. A conventional system involves a narrow band antenna to receive the scattered fields and an iterative tomographic imaging algorithm in order to achieve diffraction limited resolution. The proposed approach involves a wide band antenna coupled with a metamaterial lens and a non-iterative time reversal imaging algorithm in order to achieve rapid, sub-wavelength inspection

Manuscript received December 23, 2018; accepted February 27, 2019. Date of publication March 7, 2019; date of current version June 4, 2019. This work was supported in part by the National Science Foundation, through the Manufacturing USA program, under Award 1762331, and in part by the Italian MIUR Program through the Dipartimenti di Eccellenza 2018-2022. The associate editor coordinating the review of this paper and approving it for publication was Prof. Pai-Yen Chen. *(Corresponding author: Saptarshi Mukherjee.)*

S. Mukherjee is with the Lawrence Livermore National Laboratory, Livermore, CA 94550 USA (e-mail: mukher40@msu.edu).

Z. Su is with the Hitachi Automotive Products Research Laboratory, Farmington Hills, MI 48335 USA.

L. Udpa, S. Udpa, and A. Tamburrino are with the Nondestructive Evaluation Laboratory, Michigan State University, East Lansing, MI 48824 USA.

Digital Object Identifier 10.1109/JSEN.2019.2903454

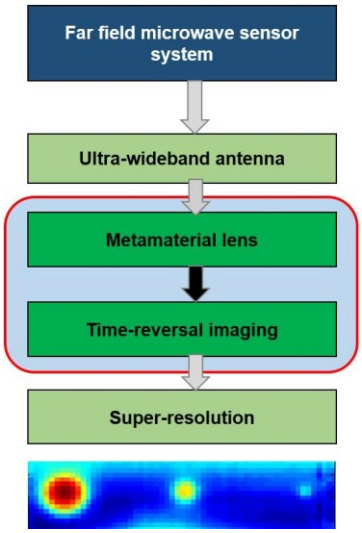

Fig. 1. Modules of a far field microwave sensor system.

of composite materials. While the authors have previously developed the antenna system [22] and the time reversal algorithm [10], the significance of the metamaterial lens has been investigated in this paper. The addition of the lens in the overall sensor system provides significant benefits such as improved focusing, rapid inspection and super-resolution. Simulation studies demonstrate the capability of the lens for focusing fields inside the composite material. Initial results using the lens, coupled with the TR imaging algorithm illustrate the superior focusing, detection and imaging resolution with far field microwave data. The paper is organized as follows. Sections 2 and 3 describe the conventional microwave imaging setup and experimental results using a passive TR algorithm to detect defects in composites. The limitations of the system in terms of resolution are presented. Sections 4 and 5 discuss the physics, numerical modeling and simulation studies of metamaterials. Section 6 couples microwave TR with the metamaterial lens and presents simulation results. The superior imaging quality and better resolution obtained with the metamaterial lens for detection of source, dielectric targets and closely spaced sub-wavelength defects inside composites demonstrate the benefits of the proposed approach using metamaterial lens in microwave NDE.

II. Principles of Time Reversal Imaging

TR is a consequence of the wave reciprocity property. The scalar wave equation in a lossless medium is given by [23]

$$\nabla^2 - \frac{n^2(r)}{c^2}\frac{\partial^2}{\partial t^2}\quad \phi(r, t) = 0. \tag{1}$$

Since the above electromagnetic wave equation is time-symmetric, the above equation yields a diverging, causal solution $\phi(r, t)$ and a converging, anti-causal solution $\phi(r, -t)$. Due to this property, the scattered fields from a point source collected by the receiver antenna array can be time reversed and back propagated using a numerical model to focus back

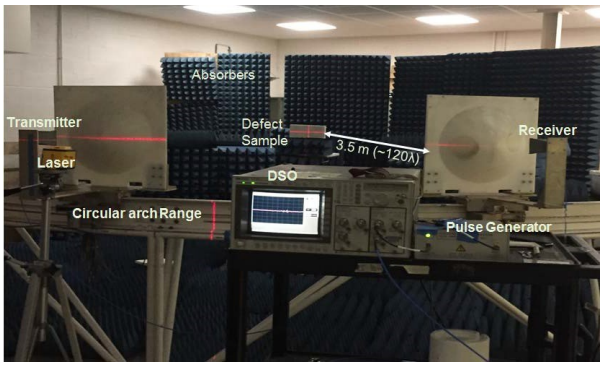

Fig. 2. Pulsed time domain experimental setup.

at the source location. This process can be modified for NDE applications in order to image defects in dielectric materials, as outlined below [24].

1) an ultra-wide band pulse is transmitted from a antenna to the region of the sample;
2) scattered signals due to the defective sample and healthy sample are measured by receivers placed at separate locations and subtracted to obtain the perturbation signal;
3) the perturbation signal waveform is reversed in time and back propagated through the healthy sample using a numerical model;
4) localization techniques are applied to obtain spatio-temporal focusing and imaging of defects in the sample.

The wave propagation phenomenon is numerically modeled for a two-dimensional TMz mode excitation by discretization of Maxwell's equations using the finite difference time domain technique, with convolution perfectly matched layer (CPML) boundary conditions to truncate the computational domain. The FDTD parameters satisfy Courant's stability criterion and are defined as follows: $\Delta x = \Delta y = \lambda/10$, $\Delta t \leq \Delta x/2c$, where Δx, Δy and Δt are the FDTD cell sizes and time steps respectively [25]. A time integrated energy localization method is utilized to obtain the focused TR energy and used as a measure of the imaging quality. Simulation results and parametric analysis have been conducted as part of prior research and have helped us determine the feasibility and limits of the parameters that affect the TR algorithm [10]. These parameters are used for conducting passive TR experiments to image defects in composite materials.

III. Problem Statement

The experimental results demonstrated in this section illustrate the limitations and issues of a conventional far field microwave imaging system. A microwave far field, bi-static, pulsed time domain experimental system is utilized to perform TR imaging for detecting defects in composite materials. The experimental setup is shown in Fig. 2. Two H-1498 horn antennas with a bandwidth from 2-18 GHz are chosen as the transmitting and receiving antennas. The antennas are mounted on a reflectivity arch-range, with the transmitter position stationary and the receiver is moved by 2° over an

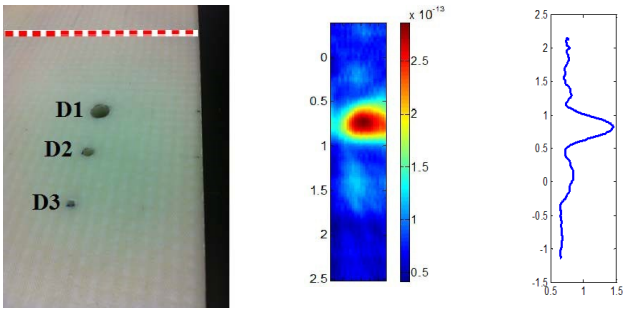

Fig. 3. Conventional TR imaging results (a) GFRP sample with defects (Red line shows healthy region), (b) Measured TR energy, (c) Cross range signal detects D1 and D2.

angular coverage of 40° in order to mimic an antenna array system. A pulse generator produces a 45 ps input pulse, which is fed to the transmitting antenna. The sample is placed in far field at a distance of 3.5 m away from the antennas. A digital sampling oscilloscope is used to measure the received back-scattered fields from the test sample and an equivalent healthy sample. The experimental system is explained in detail in [17]. The received fields from healthy and test samples are subtracted to obtain the perturbation signal which are back-propagated using the 2D TR numerical model.

The model based TR system is initially validated for imaging well defined defects in calibration and prototype samples. Next, the system is used for inspection of glass fiber reinforced polymer (GFRP) composite samples, fabricated at the MSU Composite Vehicle Research Center. A vacuum assisted resin infusion technique was used to manufacture the samples with S2-glass plain weave fabric (fibers woven at 0 and 90°). The composite sample (Fig. 12(a)) is a sixteen layer cured laminate with a thickness of 9 mm. 3 holes of radius 4 mm (D1), 2 mm (D2), and 1 mm (D3), separated from each other by an inch were drilled, as shown in Fig. 3 (a). The perturbation signals were measured, reversed in time and back-propagated in the numerical model. As shown in Fig. 3 (b), the integrated energy image is capable of detecting the two bigger defects (D1 and D2), but D3 is not detected. This is due to the fact that the far field microwave data is limited by the classical diffraction theory, thus producing a focal spot of the order of the operating wavelength [23]. The cross range signal shown in Fig. 3 (c) indicates strong detection of the 4 mm radius hole, a relatively weak detection of the 2 mm radius hole and no detection of the 1 mm radius hole, since the time reversed wave focuses back with an amplitude proportional to the scattering cross sectional area of the defects. While there are several types of practical defects in composites such as disbonds and fiber delaminations that are smaller than 1 mm, the current experimental setup is limited to imaging defects of size more than 4 mm ($\lambda/4$). A potential solution for this issue is offered by metamaterials, which are discussed in the following sections.

IV. Metamaterials

Metamaterials are artifical materials designed using periodic structures to create a desired macroscopic behavior such as negative index of refraction. Due to their unique properties, research on metamaterials has increased in terms of both theory and applications. The simultaneous negative permittivity and permeability of the metamaterial results in a negative refractive index. The refractive index of metamaterials is given by [26]

$$n = -\sqrt{\mu\varepsilon}. \tag{2}$$

Maxwell's curl equations for a monochromatic plane wave in k-space is given by:

$$k \times \mathbf{H} = -\frac{\omega\varepsilon}{c}\mathbf{E}; \quad k \times \mathbf{E} = \frac{\omega\mu}{c}\mathbf{H}. \tag{3}$$

It can be clearly seen that E,H and k form a left handed triplet of vectors for LHMs (in contrary to a right handed triplet for conventional materials), which result in the phase velocity being anti-parallel to the group velocity. The energy flux carried by the wave is determined by the Poynting vector S, given by

$$S = \frac{c}{4\pi}\mathbf{E} \times \mathbf{H}. \tag{4}$$

Thus, the vector S always forms a right handed set with the vectors E and H. Accordingly in right handed substances, S and k are in the same direction. In left handed substances, S and k are in the opposite direction. Since k is associated with phase velocities, we can observe that the phase velocity and group velocity are in opposite directions in LHM. The phase velocity is opposite in direction to the energy flux, leading to several phenomenon such as reversed Doppler and reversed Vavilov-Cerenkov effects [27], [28].

The negative refractive index of metamaterials can be utilized in the design of a planar lens that can achieve perfect focusing, thus focusing the radiation from a point source located at a distance d_1 from the plate [21]. The lens can achieve resolution beyond the diffraction limit. Additionally, the evanescent fields that are not transmitted in a conventional lens can be recovered in a metamaterial region due to its negative refractive index [29]. This can be mathematically understood by defining a wave propagating along +z direction described by a superposition of elementary plane waves of the type:

$$E(x, y, z; t) = \sum_{k_x, k_y} A(k_x, k_y) e^{j(k_x x + k_y y + k_z z - \omega t)}, \tag{5}$$

where $k_z = \sqrt{\frac{\omega^2}{c^2} - k_x^2 - k_y^2}$ is real, leading to propagating waves, when $\frac{\omega^2}{c^2} > (k_x^2 + k_y^2)$. However, k is imaginary, when $\frac{\omega^2}{c^2} < (k_x^2 + k_y^2)$, leading to the high angular frequency evanescent waves. In a conventional lens, the evanescent wave amplitude decays exponentially along z axis from the source location, giving a highest resolution of $k_{max} = 2\pi/\lambda$. However, in order to transport energy along positive y axis in a metamaterial region, $k_z = -\sqrt{\frac{\omega^2}{c^2} - k_x^2 - k_y^2}$. The evanescent fields (small scale features) are amplified in the metamaterial region. Thus they can be recovered, enhanced and transmitted, leading to super-resolution. Thus, while the resolution of a conventional lens based on materials with

positive refractive index and curved surfaces is limited by the operating wavelength, the super resolution property of the metamaterial lens can transcend diffraction limits and is capable of sub-wavelength resolution with increased overall sensitivity.

In 1967, Veselago [26] formulated the negative refraction capability of metamaterials mathematically by matching boundary conditions for E and H fields. Over the past 2 decades, a lot of research has been focused in the physical design of a metamaterial lens [30]–[32]. The research conducted in the following sections involve simulations that consider homogenization of metamaterials based on Veselago's ideas. In other words, the simulation studies are conducted considering the metamaterial region as a homogeneous medium with equivalent permeability and permittivity expressions.

A. Electromagnetic Properties of the Metamaterial

Metamaterials are characterized by a double negative (DNG) layer can be described using electromagnetic plasma equations. The ideal dielectric response of a plasma is given by

$$\varepsilon = \varepsilon_0 \left(1 - \frac{\omega_{pe}^2}{\omega^2}\right), \tag{6}$$

which takes negative values for $\omega < \omega_{pe}$, where ω_{pe} is the peak electric plasma frequency. The ideal magnetic response of a plasma is given by

$$\mu = \mu_0 \left(1 - \frac{\omega_{pm}^2}{\omega^2}\right), \tag{7}$$

which takes negative values for $\omega < \omega_{pm}$, where ω_{pm} is the peak magnetic plasma frequency. Tuning these parameters, it is possible to attain a value of $\varepsilon = -1$ and $\mu = -1$ atleast at a single frequency. The frequency dispersive electric and magnetic properties of a lossy Drude model characterizing the DNG layer can thus be expressed as [33]

$$\varepsilon(\omega) = \varepsilon_0 \left(1 + \frac{\omega_{pe}^2}{\omega_{oe}^2 - \omega^2 + j\tau_e\omega}\right);$$
$$\mu(\omega) = \mu_0 \left(1 + \frac{\omega_{pm}^2}{\omega_{om}^2 - \omega^2 + j\tau_m\omega}\right), \tag{8}$$

where ε_0 and μ_0 are the free space permittivity and permeability, ω_{oe}, ω_{om} are the frequency edge of electric and magnetic plasma and τ_e, τ_m refer to electric and magnetic losses due to the electric and magnetic collision. It can be easily found out from the above equations that $\varepsilon < 0$ when $\omega_{oe} < \omega < \omega_{pe}$ and $\mu < 0$ when $\omega_{om} < \omega < \omega_{pm}$. The refractive index for the parameter values of $\omega_{pm} = \omega_{pe} = 20$ GHz, $\omega_{om} = \omega_{oe} = 4$ GHz and $\tau_e = \tau_m = 0$ to be used in later simulations, are shown in Fig. 4.

B. Numerical Modeling of the DNG Layer

As mentioned in Section II, FDTD is used for numerical modeling of Maxwell's equations. Using the frequency dispersive electromagnetic properties shown in (8), the electric

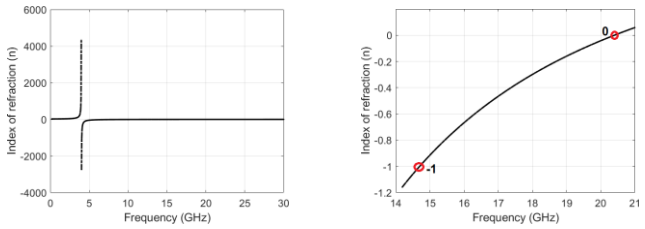

Fig. 4. (a) Refractive index of a DNG medium, (b) zoomed in plot shows n = −1 and zero crossover point.

constitutive relationship can be modified in the presence of the DNG layer as follows:

$$D(\omega) = \varepsilon_0 E(\omega) + P(\omega),$$
$$P(\omega) = \frac{\varepsilon_0 \omega_{pe}^2}{\omega_{oe}^2 - \omega^2 + j\tau_e\omega} E(\omega), \tag{9}$$

where $E(\omega)$, $D(\omega)$ and $P(\omega)$ are the electric field, displacement current and polarization density of the medium respectively. Since the fields are modeled in time domain, the frequency dependent terms of (9) need to be converted to equivalent terms in time domain. The auxiliary differential equation (ADE) method uses inverse Fourier Transform to convert frequency domain equations into corresponding time domain difference equations, given by

$$j\omega P(\omega) \leftrightarrow \frac{(P^n - P^{n-2})}{2\Delta t},$$
$$(j\omega)^2 P(\omega) \leftrightarrow \frac{(P^n - 2P^{n-1} + P^{n-2})}{\Delta t^2},$$
$$P(\omega) \leftrightarrow P^{n-1} \tag{10}$$

Using the above relations in (9) along with the central difference approximation method, the fields are updated by time marching algorithm as follows:

$$\omega_{oe}^2 P^{n-1} + \frac{(P^n - 2P^{n-1} + P^{n-2})}{\Delta t^2} - \tau_e \frac{(P^n - P^{n-2})}{2\Delta t} = \varepsilon_0 \omega_{pe}^2 E^{n-1} \tag{11}$$

Arranging like terms the final updating equation for $P(\omega)$, with the fields updated recursively by FDTD is given by

$$P^n = \frac{\frac{2}{\Delta t^2} - \omega_{oe}^2}{\frac{\tau_e}{2\Delta t} + \frac{1}{2\Delta t}} P^{n-1} + \frac{\frac{\tau_e}{2\Delta t} - \frac{1}{2\Delta t}}{\frac{\tau_e}{2\Delta t} + \frac{1}{2\Delta t}} P^{n-2} + \frac{\omega_{pe}^2 \varepsilon_0}{\frac{\tau_e}{2\Delta t} + \frac{1}{\Delta t^2}} E^{n-1}. \tag{12}$$

In a similar fashion, the magnetic fields inside a DNG layer can be solved by recursively updating the magnetic polarization density, with the fields updated recursively by FDTD. A simple 2D FDTD scheme was used to solve for electromagnetic fields in the Double Positive Region (DPS).

In order to understand and validate the wave propagation in the presence of the metamaterial slab, wave propagation simulations are conducted in a DPS-DNG-DPS medium with the schematic and spatial dimensions shown in Fig. 5 (a).

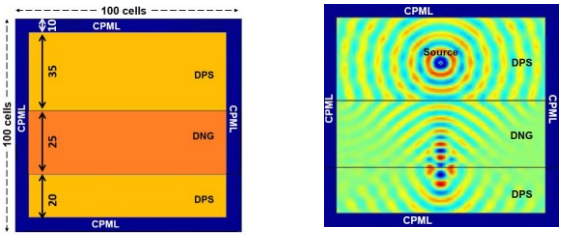

Fig. 5. DPS-DNG-DPS interface: (a) simulation schematic, (b) wave propagation.

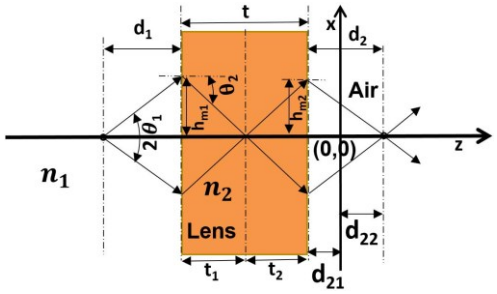

10 cells are chosen for the convolution perfectly matched layer (CPML) boundaries, with a 25 cell thick DNG slab (cells 45 to 70) inserted between the DPS regions. An input sinusoidal pulse with central frequency $f_0 = 14.7$ GHz was chosen with n = −1. Fig. 5 (b) shows the electric field snapshot at T = 300 of the electromagnetic wave. The waves undergo a phase reversal of 180° at the first DPS-DNG interface and another phase reversal of 180° at the second DPS-DNG interface. Thus Fig. 5 (b) shows negative phase velocity (backward propagation) in the DNG region and positive phase velocity (forward propagation) in the DPS region, as expected in a typical metamaterial behavior.

V. Focusing of Fields Using the Lens

The DNG layer can be utilized in the design of a metamaterial lens with perfect refocusing capabilities.

A. Focusing of the Lens in Free Space

It can be shown in Fig. 6 that the radiation from a point source located at a distance (d_1) from the lens can focus at a point (d_2) in free space. If the thickness (t) of the DNG layer is appropriately chosen, the electromagnetic fields are refracted in the DPS-DNG interfaces such that the field focuses once inside the lens and once outside the lens. The lens thickness t can be chosen according to the following relationship, d_1 d_2 t and the corresponding ray diagram shown in Fig. 6. This relationship can be derived from the ray diagram as follows:

$$h_{m1} = d_1\tan\theta_1;\ h_{m1} = t_1\tan\theta_2;$$
$$h_{m2} = d_2\tan\theta_2;\quad h_{m2} = t_2\tan\theta_2; \tag{13}$$

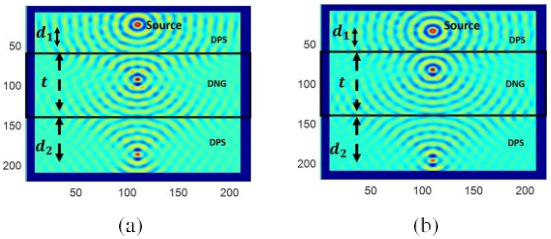

Fig. 7. Focusing of the metamaterial lens in free space: (a) $d_1 = 3.5\ \lambda_0$; $d_2 = 4.4\ \lambda_0$; t = $8\lambda_0$, (b) $d_1 = 2.4\ \lambda_0$; $d_2 = 5.5\ \lambda_0$; t = $8\lambda_0$.

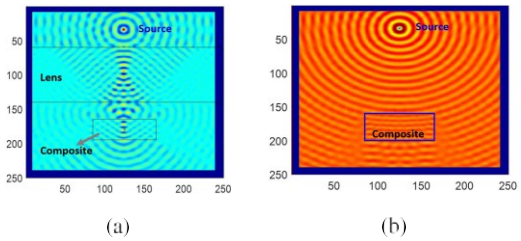

Fig. 8. Focusing nature of the metamaterial lens in composites: (a) Focused wave with lens, (b) Near plane wave without lens.

where all the parameters h_{m1}, h_{m2}, t_1, t_2 are defined in the ray diagram. Combining the above equations, we obtain

$$d_1 = t_1\tan\theta_2\cot\theta_1\ d_2 = t_2\tan\theta_2\cot\theta_1;$$
$$d_1 + d_2 = (t_1 + t_2)\tan\theta_2\cot\theta_1. \tag{14}$$

From Snell's law we obtain a relationship between θ_1 and θ_2.

$$\sin\theta_1 = |n_2|\sin\theta_2, \tag{15}$$

where n_2 is the refractive index of the metamaterial lens. Combining (14) and (15), the relationship between d_1, d_2 and t is obtained.

$$d + \quad g = t \frac{\cos\theta_1}{\sqrt{n_2^2 - \sin^2\theta_1}} \quad . \tag{16}$$

It can be observed that for a perfect metamaterial lens ($n_2 = -1$), (16) is reduced to d_1 d_2 t. =

FDTD simulations are conducted with the sinusoidal excitation source in order to validate the focusing property of the lens with the chosen parameters d_1 3.5 λ_0 and 8λ_0. The electric fields shown in Fig. 7 (a), shows the first focal spot inside the lens and the second focal spot outside the lens, with d_2 = 4.4 λ_0, which satisfies the perfect focusing condition. It can be observed from (16), that keeping the thickness of the lens constant, varying d_1 produces the second focal spots at different d_2 position. When d_1 is 2.5 λ_0, d_2 is found out to be 5.4 λ_0, as seen in Fig. 7 (b).

B. Focusing in Presence of a Composite

The simulations described above show that the lens has perfect focusing capabilities in free space. This section studies its focusing capability in presence of a composite sample.

FDTD simulations are conducted with the sinusoidal excitation source at 14.7 GHz in the presence of the lens and a composite sample with $\varepsilon_r = 4$. The simulation parameters

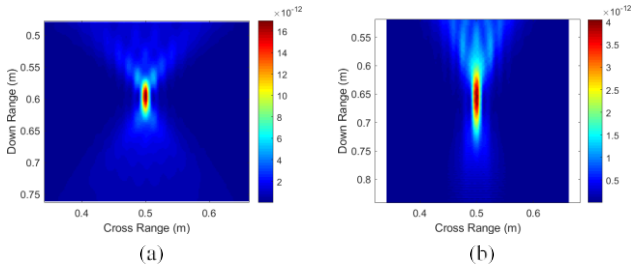

Fig. 9. Focusing resolution of the lens (a) free space, (b) composite.

are as follows $d_1 = 3.5\lambda_0$, $d_2^1 = 3.5\lambda_0$ and $t = 8\lambda_0$. The dimension of the composite is $4\lambda_0 \times 8\lambda_0$. In the presence of the lens, the waves focus once inside the lens, refract at the composite interface and later focus in a region inside the composite, as seen in Fig. 8(a). Fig. 8(b) shows that in the absence of the lens, near plane waves are incident on the composite, which limits the imaging resolution.

1) Resolution of Focal Spot: The focal spot of the metamaterial lens in the presence of the composite needs to be studied in order to assess the imaging resolution of the lens. The focusing resolution is determined from the integrated energy of the focused wave on the composite and is plotted in Fig. 9. In the absence of the composite sample, there is no additional refraction and all rays combine at the same point, leading to an ideal focal spot with near equal cross and down range resolutions, as shown in Fig. 9 (a). In the presence of the composite, the rays constituting the EM wave are refracted at different angles at the air-composite interface. Thus although all the rays focus at the same cross range location, they are focused at different down-range depth regions of the composite sample. From Fig. 9 (b), it can be clearly seen that the wave is localized well along the cross range, but poorly localized along the down range. Due to the poor down-range resolution, defects situated along down range will be more difficult to detect and resolve than along the cross range.

2) Location of Focal Spot Inside the Sample: The ray diagrams through the lens in free space and the presence of a composite half space are shown in Fig. 10. The ray undergoes an additional refraction at the composite interface in accordance with Snell's law. Since the wave velocity inside the composite is slower than free space, scaled by the composite's relative dielectric constant, the wave is focused at a distance d_2^1 from the lens instead of d_2 ($d_2^1 > d_2$). The ray diagrams can be utilized to determine the location of the second focus of fields inside the composite sample. From the simple ray diagrams in Fig. 10 and application of Snell's law, we have,

$$d_2 = d_{21} + d_{22};\ d^1 = d_{21} + d_{22}^1. \tag{17}$$

Using Snell's law of refraction at the air-composite interface for Fig. 10 (a), we obtain

$$\frac{\sin\theta_1}{\sin\theta_3} = \frac{n_3}{n_1} = \sqrt{\varepsilon_r}. \tag{18}$$

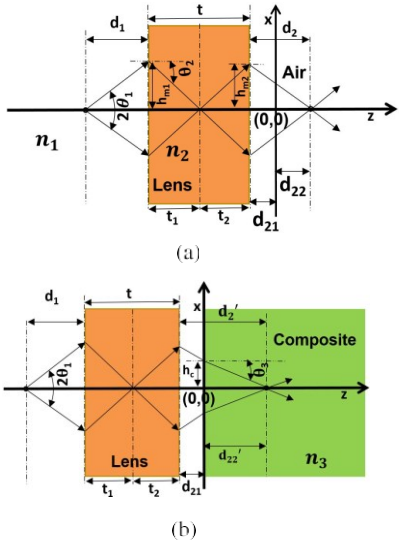

Fig. 10. Ray diagram of metamaterial lens in the presence of (a) air, (b) composite half space.

Additionally using simple trigonometric identities from Fig. 10, we obtain

$$\frac{h_c/2}{d_{22}^1} = \tan\theta_3, \quad \frac{h_c/2}{d_{22}} = \tan\theta_1. \tag{19}$$

Combining the above two equations, we obtain

$$\frac{d_{22}^1}{d_{22}} = \frac{\tan\theta_1}{\tan\theta_3}. \tag{20}$$

From (20) and (17), d_{22}^1 can be calculated as

$$d_{22}^1 = d_{22}\ \tan\theta_1 \cot\theta_3 \tag{21}$$

Combining (18) and (21), we get the analytical expression of d_{22}^1 and determine the exact focusing spot in terms of d_{22}, ε_r and θ_1, as follows:

$$d_{22}^1 = d_{22}\ \frac{\sqrt{\varepsilon_r - \sin^2\theta_1}}{\cos\theta_1}. \tag{22}$$

It is observed from (22) that $d_{22}^1 = d_{22}$, when $\varepsilon_r = 1$, leading to a focal point at d_2 in free space. However, since the wave consists of a bundle of rays incident at different angles, θ_1 depends on the radiation pattern and beamwidth of the antenna that is used as the source. Thus finding the exact focusing distance is non trivial from (22). Using a small angle approximation and combination of (18) and (20), the relationship between d_{22} and d_{22}^1 can be approximated simply in terms of ε_r as follows,

$$\frac{d_{22}^1}{d_{22}} = \sqrt{\varepsilon_r}. \tag{23}$$

The derived expression is compared with numerical FDTD simulations in order to determine the approximation error. For a dielectric sample of $\varepsilon_r = 4$ ($d_{22}^1 = 2\ d_{22}$), Fig. 11 shows good comparison between the simulation results and results obtained from (23), the error being around ~5%. (23) gives an important yet simple approximate relationship between

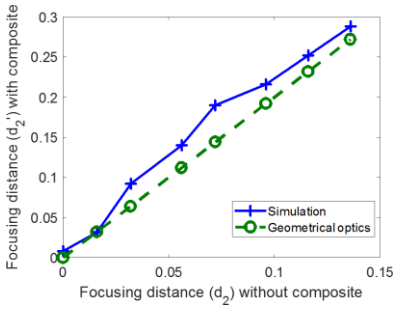

Fig. 11. Comparison between geometrical optics theory and simulation for determining focusing distance.

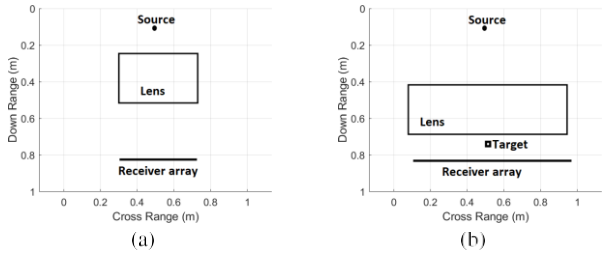

Fig. 12. Schematic of test geometry: (a) source, (b) target.

d_{22} and d_{22}^{1}. If the bulk dielectric constant of the sample to be inspected can be extracted from a material characterization technique, (23) can be utilized to determine an approximate location where the field will be focused in the sample.

VI. Time Reversal With Metamaterial Lens

The previous section demonstrates the capability of the metamaterial sensor for focusing in free space as well as in composites. Next, the metamaterial lens is coupled with the far field TR imaging algorithm, for achieving high resolution imaging. TR back-propagation simulations based on a transmission mode setup are conducted for detecting the excitation source, sub-wavelength targets and defects embedded inside a composite. The input pulse s(t) is a modulated Gaussian pulse of pulse width 73 ps, corresponding to a 12 GHz bandwidth having a modulating frequency $f_0 = 14.7$ GHz,

$$s(t) = e^{-\frac{(t-t_0)^2}{2\sigma^2}} \cos(2\pi f_0 t), \tag{24}$$

where the Gaussian pulse is centered at t_0 and σ determines the pulse width.

A. Source Detection in Air

Simulations are conducted to image a source in transmission mode with and without the metamaterial lens. The metamaterial lens is placed between the source and the receiver array, as shown in Fig. 12 (a). The electric fields are measured by the receiver array, time reversed and back-propagated numerically. The time reversed energy images with and without the lens are shown in Figs. 13 (a, b). It is observed that the TR energy is much more focused in cross and down range directions in the presence of the lens. The evanescent field amplification and perfect focusing condition of the lens is responsible for

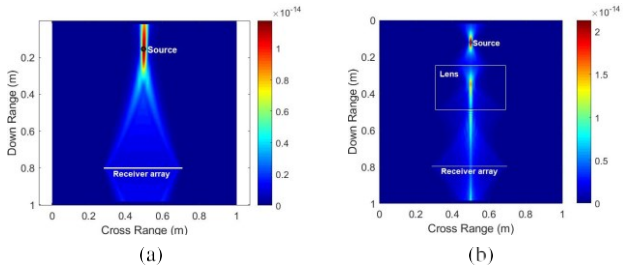

Fig. 13. TR with metamaterial lens shows enhancement of microwave imaging for source imaging, (a) TR energy without metamaterial lens, (b) TR energy with lens.

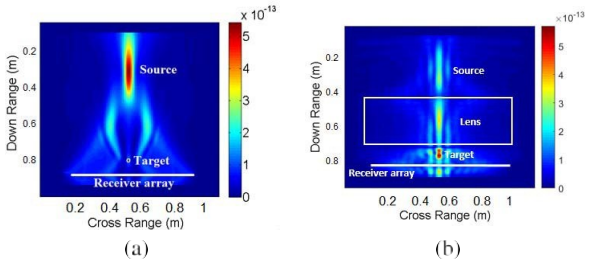

Fig. 14. TR with metamaterial lens shows enhancement of microwave imaging for sub-wavelength target imaging, (a) TR energy without metamaterial lens, (b) TR energy with lens.

the superior resolution of the image. Although a focal spot is detected in the lens and additional artifacts are observed at the lens interface, they are relatively far away from the source position and to affect the imaging resolution of the lens.

B. Target Detection in Air

Next the capability of the metamaterial lens for detecting sub-wavelength targets is demonstrated. A sub-wavelength square target of size 2 mm ($\lambda_0/10$) and relative dielectric constant of 4 is placed with and without the lens as shown in Fig. 12 (b). The electric fields are measured by the receiver array in the presence and absence of the target and subtracted in order to calculate the perturbation fields. The perturbation signals are time reversed and back-propagated numerically in the model. The time reversed energy with and without the lens is shown in Figs. 14 (a, b). It can be clearly observed that while the TR energy is efficiently localized on the small target with the lens, there is hardly any focusing in its absence. Although additional artifacts are observed at the lens interface with focal spots within the lens and source position, they are relatively far away from the dielectric target region and does not affect the imaging resolution. The cross range signal (Fig. 15) shows the superior focusing and sub-wavelength target detection capability of the imaging system.

C. Defect Detection in Composites

Next, the lens is used for detecting closely spaced subsurface, sub-wavelength defects inside a composite slab. Several cases involving multiple defects closely separated in the cross range and down range directions are studied. The spatial dimensions of the metamaterial lens used for simulations are 16 cm $\times$ 6 cm ($8\lambda_0 \times 3\lambda_0$).

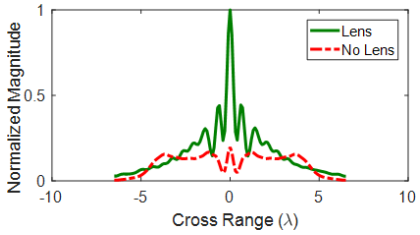

Fig. 15. Cross range signal of target with and without lens.

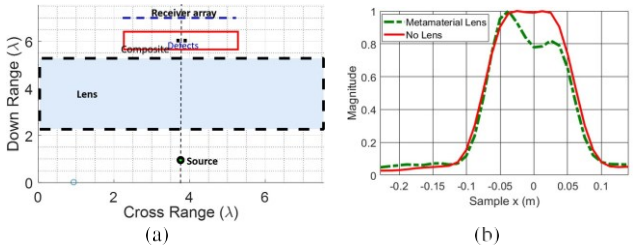

Fig. 16. TR with metamaterial lens shows enhancement of microwave imaging for sub-wavelength cross range separated sub-wavelength defects in a composite slab, (a) Schematic of test geometry, (b) TR energy comparison.

1) Cross Range Separated Defects: A GFRP slab of dimensions 6 cm×5 mm ($3\lambda_0 \times \lambda_0/4$) is placed between the metamaterial lens and the receiver array, as shown in Fig. 16(a). Two sub-wavelength square air voids (D1 and D2) of size 2 mm ($\lambda_0/10$) are placed in the middle of the sample, separated in cross range by a distance of 2 mm ($\lambda_0/10$), as shown in Fig. 16(a). TR simulations are conducted for this configuration with and without the lens. Similar to the process mentioned in Section II, the perturbation field is extracted from signals corresponding to reference and test samples, time reversed and back-propagated in the numerical model. Important parameters t, d_1 and d_2 are chosen such that the lens focuses fields on the defect plane. It is also worth mentioning that source location and consequently the focal spot in the composite is closer to defect 1. The time reversed normalized cross range signal comparison with and without the lens is shown in Fig. 16 (b). Without the lens, the TR energy image is unable to resolve the closely spaced defects and produces an image of a single extended defect. However, in the presence of the metamaterial lens, the TR energy is able to resolve both D1 and D2 efficiently. Since the source location is closer to D1 as mentioned before, the focal spot in the composite is closer to D1 and thus more electromagnetic energy interacts with D1 than D2. Thus, although both defects are of same size, higher TR energy is focused on D1.

The focusing spot inside the composite can be shifted in the horizontal plane by translating the source. In order to understand this effect, the source is moved to 6 different positions as shown in Fig. 17(a) and the corresponding normalized TR energy results are displayed in Fig. 17(b). From Fig. 17 (b), it is clearly observed that the back-propagated TR energy image of a defect reduces as the focal spot shifts further away from the defect. At position 4, minimum energy is focused on defect 2, as it is farthest from the source and is thus exposed to relatively lower electromagnetic fields. Similarly, at position 6,

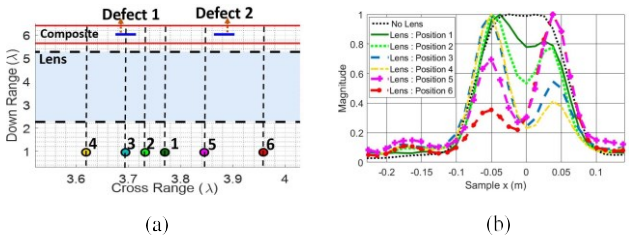

Fig. 17. TR with metamaterial lens shows enhancement of microwave imaging for sub-wavelength cross range separated sub-wavelength defects in a composite slab, (a) Schematic of test geometry, (b) TR energy comparison.

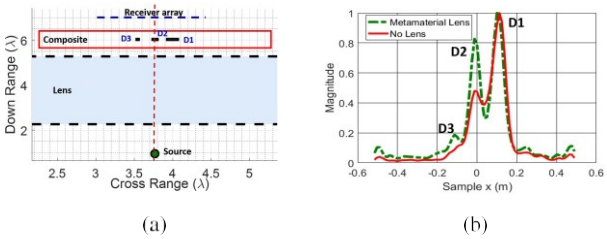

Fig. 18. TR with metamaterial lens shows enhancement of microwave imaging for a sub-wavelength defects in a composite slab for different source positions, (a) Schematic of test geometry, (b) TR energy comparison.

minimum energy is focused at defect 1, as it is farthest from the source. The implication of this results is that one can focus the energy to any desired location in the composite to obtain a high resolution image of the composite sample.

A far field experiment with TR processing was performed previously for detecting 3 drilled holes in a GFRP sample (shown in Fig. 18 (a)). Finally, we consider a similar sample discussed in Section III with three defects (D1, D2 and D3) of dimensions 1 cm×4 mm ($\lambda_0/2 \times \lambda_0/5$), 4 mm 4×mm ($\lambda_0/5 \times \lambda_0/5$) and 2 mm × 4 mm ($\lambda_0/10 \times \lambda_0/5$), separated in cross range by a distance of 4 mm ($\lambda_0/5$), as shown in Fig. 18(a). TR simulation results with and without the metamaterial lens are shown in Fig. 18 (b). Without the metamaterial lens, the TR energy is able to clearly detect D1 and weakly detects D2, but D3 is undetected. However in the presence of the metamaterial lens, the TR energy is able to clearly detect all three defects with the strongest indication of D1 followed by D2 and D3 due to its super resolution capabilities. The results indicate that if a physical metamaterial lens is utilized, the resolution of far field microwave imaging can be enhanced.

2) Down Range Separated Defects: As described earlier, the focal spot of the lens is sharp in the cross range, but diffuse in the down range, making it harder to detect and image defects in the down range direction. The previous section demonstrated how the focal spot can be moved horizontally in the sample by moving the source. This section describes how the focal spot can be moved in the vertical direction by moving the source in the vertical direction relative to the sample. In order to understand this effect, the source is moved to 3 different positions, indicated by A,B,C as shown in Fig. 19(a). Line scans across the TR energy image obtained for the different positions are presented in Fig. 19(b). From Fig. 19 (b), it is clearly observed that the back-propagated TR

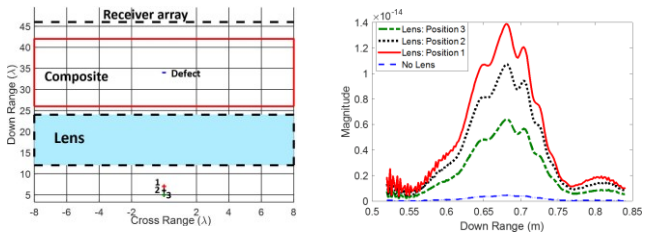

Fig. 19. TR with metamaterial lens shows enhancement of microwave imaging for sub-wavelength cross range separated sub-wavelength defects in a composite slab, (a) Schematic of test geometry, (b) TR energy comparison.

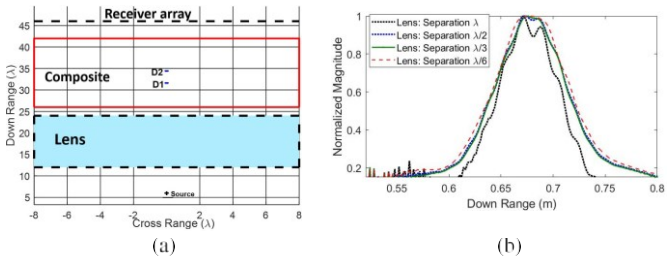

Fig. 20. TR with metamaterial lens shows enhancement of microwave imaging for sub-wavelength down range separated sub-wavelength defects in a composite slab, (a) Schematic of test geometry, (b) TR energy comparison.

energy at the defect reduces as the focal spot shifts down from the defect. Additionally, it is observed that the field amplitude with the lens (1.4×10^{-14}V/m) is approximately 28 times larger than that obtained without the lens (5×10^{-16}V/m). Thus the lens adds sensitivity and focusing property in the down range direction.

In order to determine the minimum separation between 2 defects placed in the down range, TR simulations are conducted for varying separation distances as shown in Fig. 20(a) and the corresponding results are displayed in Fig. 20(b). While the minimum detectable cross range separation between defects for detection is noted to be $\lambda_0/10$, the minimum detectable down range separation for detection between defects is estimated to be $\lambda_0/3$.

The above results demonstrate that a metamaterial lens can be used in conjunction with TR to improve the microwave imaging resolution. Better detection of sub-wavelength targets and higher resolution with superior focusing is achieved using the lens. Simulation results also indicate much more improvement in cross range resolution ($\lambda_0/10$) than the down range resolution.

VII. Conclusion

A metamaterial lens based sensor system is proposed for enhancement of microwave imaging for NDE of composites. Model based time reversal imaging experiments are performed in order to image practical defects in GFRP samples. The far field system limits the imaging resolution and paves the way for the design of a metamaterial lens. Theoretical and simulation studies demonstrate ability of a DNG layer to function as a lens to achieve focusing in free space and in the presence of composites. Finally, the lens is used in conjunction with TR for detecting source, sub-wavelength targets and closely spaced sub-surface, sub-wavelength defects in composite materials. Future work in this research involves several tasks. The analytical expressions for the spread of the focusing spot needs to be derived in order to model focusing resolution and shift in a lossy, imperfect metamaterial lens. Although TR is successfully combined with the lens, all the simulations are performed in transmission mode. In several practical inspections, there is only single side access. Hence the performance of the metamaterial lens for NDE applications needs be reevaluated in reflection mode. Another task involves optimizing the operating frequency, shape and electromagnetic properties of the lens in order to improve its down-range resolution.

References

[1] H. Ku, H. Wang, N. Pattarachaiyakoop, and M. Trada, "A review on the tensile properties of natural fiber reinforced polymer composites," *Compos. B, Eng.*, vol. 42, no. 4, pp. 856–873, 2011.

[2] B. Harris, *Fatigue in Composites: Science and Technology of the Fatigue Response of Fibre-Reinforced Plastics*. Sawston, U.K.: Woodhead, 2003.

[3] R. A. Kline, *Nondestructive Characterization of Composite Media*. London, U.K.: Routledge, 2017.

[4] D. E. Bray and R. K. Stanley, *Nondestructive Evaluation: A Tool in Design, Manufacturing and Service*. Boca Raton, FL, USA: CRC Press, 1996.

[5] O. Karpenko, A. Khomenko, E. Koricho, M. Haq, and L. Udpa, "Monitoring of fatigue damage in composite lap-joints using guided waves and FBG sensors," in *Proc. AIP Conf.*, 2016, vol. 1706, no. 1, Art. no. 120005.

[6] G. Yang *et al.*, "Pulsed eddy-current based giant magnetoresistive system for the inspection of aircraft structures," *IEEE Trans. Magn.*, vol. 46, no. 3, pp. 910–917, Mar. 2010.

[7] S. Kharkovsky and R. Zoughi, "Microwave and millimeter wave nondestructive testing and evaluation—Overview and recent advances," *IEEE Instrum. Meas. Mag.*, vol. 10, no. 2, pp. 26–38, Apr. 2007.

[8] S. Bakhtiari, N. Qaddoumi, S. I. Ganchev, and R. Zoughi, "Microwave noncontact examination of disbond and thickness variation in stratified composite media," *IEEE Trans. Microw. Theory Techn.*, vol. 42, no. 3, pp. 389–395, Mar. 1994.

[9] P. Roy Paladhi, A. Tayebi, P. Banerjee, L. Udpa, and S. Udpa, "Image reconstruction from highly sparse and limited angular diffraction tomography using compressed sensing approach," *Prog. Electromagn. Res.*, vol. 158, pp. 21–36, Jan. 2017.

[10] S. Mukherjee, A. Tamburrino, M. Haq, S. Udpa, and L. Udpa, "Far field microwave NDE of composite structures using time reversal mirror," *NDT & E Int.*, vol. 93, pp. 7–17, Jan. 2018.

[11] M. Fink, "Time reversal of ultrasonic fields. I. Basic principles," *IEEE Trans. Ultrason., Ferroelectr., Freq. Control*, vol. 39, no. 5, pp. 555–566, Sep. 1992.

[12] M. Fink *et al.*, "Time-reversed acoustics," *Rep. Prog. Phys.*, vol. 63, no. 12, p. 1933, 2000.

[13] G. Lerosey, J. de Rosny, A. Tourin, A. Derode, G. Montaldo, and M. Fink, "Time reversal of electromagnetic waves," *Phys. Rev. Lett.*, vol. 92, no. 19, p. 193904, May 2004.

[14] R. C. Qiu, C. Zhou, N. Guo, and J. Q. Zhang, "Time reversal with miso for ultrawideband communications: Experimental results," *IEEE Antennas Wireless Propag. Lett.*, vol. 5, no. 1, pp. 269–273, Dec. 2006.

[15] P. Kosmas and C. M. Rappaport, "Time reversal with the FDTD method for microwave breast cancer detection," *IEEE Trans. Microw. Theory Techn.*, vol. 53, no. 7, pp. 2317–2323, Jul. 2005.

[16] B. E. Henty and D. D. Stancil, "Multipath-enabled super-resolution for RF and microwave communication using phase-conjugate arrays," *Phys. Rev. Lett.*, vol. 93, no. 24, 2004, Art. no. 243904.

[17] S. Mukherjee, L. Udpa, S. Udpa, and E. J. Rothwell, "Target localization using microwave time-reversal mirror in reflection mode," *IEEE Trans. Antennas Propag.*, vol. 65, no. 2, pp. 820–828, Feb. 2017.

[18] Y. Deng and X. Liu, "Electromagnetic imaging methods for nondestructive evaluation applications," *Sensors*, vol. 11, no. 12, pp. 11774–11808, 2011.

[19] D. Shreiber, M. Gupta, and R. Cravey, "Microwave nondestructive evaluation of dielectric materials with a metamaterial lens," *Sens. Actuators A, Phys.*, vol. 144, no. 1, pp. 48–55, 2008.
[20] D. Shreiber, M. Gupta, and R. Cravey, "Comparative study of 1-D and 2-D metamaterial lens for microwave nondestructive evaluation of dielectric materials," *Sens. Actuators A, Phys.*, vol. 165, no. 2, pp. 256–260, 2011.
[21] J. Pendry, "Negative refraction makes a perfect lens," *Phys. Rev. Lett.*, vol. 85, no. 18, p. 3966, 2000.
[22] S. Mukherjee, L. Udpa, Y. Deng, P. Chahal, and E. J. Rothwell, "Design of a microwave time reversal mirror for imaging applications," *Prog. Electromagn. Res. C*, vol. 77, pp. 155–165, Sep. 2017.
[23] J. de Rosny, G. Lerosey, and M. Fink, "Theory of electromagnetic time-reversal mirrors," *IEEE Trans. Antennas Propag.*, vol. 58, no. 10, pp. 3139–3149, Oct. 2010.
[24] S. Mukherjee, A. Tamburrino, L. Udpa, and S. Udpa, "NDE of composite structures using microwave time reversal imaging," in *Proc. 42nd Annu. Rev. Prog. Quant. Nondestruct. Eval.*, vol. 1706, 2016, Art. no. 100002.
[25] K. Yee, "Numerical solution of initial boundary value problems involving Maxwell's equations in isotropic media," *IEEE Trans. Antennas Propag.*, vol. AP-14, no. 3, pp. 302–307, May 1966.
[26] V. G. Veselago, "The electrodynamics of substances with simultaneously negative values of ε and μ," *Sov. Phys.-Usp.*, vol. 10, no. 4, p. 509, 1968.
[27] S. H. Lee, C. M. Park, Y. M. Seo, and C. K. Kim, "Reversed Doppler effect in double negative metamaterials," *Phys. Rev. B, Condens. Matter*, vol. 81, no. 24, 2010, Art. no. 241102.
[28] E. S. Belonogaya, S. N. Galyamin, and A. V. Tyukhtin, "Properties of Vavilov–Cherenkov radiation in an anisotropic medium with a resonant dispersion of permittivity," *J. Opt. Soc. Amer. B, Opt. Phys.*, vol. 28, no. 12, pp. 2871–2878, 2011.
[29] D. R. Smith, J. B. Pendry, and M. C. K. Wiltshire, "Metamaterials and negative refractive index," *Science*, vol. 305, no. 5685, pp. 788–792, 2004.
[30] J. B. Pendry and S. A. Ramakrishna, "Refining the perfect lens," *Phys. B, Condens. Matter*, vol. 338, nos. 1–4, pp. 329–332, 2003.
[31] K. Aydin, I. Bulu, and E. Ozbay, "Subwavelength resolution with a negative-index metamaterial superlens," *Appl. Phys. Lett.*, vol. 90, no. 25, 2007, Art. no. 254102.
[32] N. Kundtz and D. R. Smith, "Extreme-angle broadband metamaterial lens," *Nature Mater.*, vol. 9, no. 2, pp. 129–132, 2010.
[33] C. Goswami, S. Mukherjee, S. Karmakar, M. Pal, and R. Ghatak, "FDTD modeling of Lorentzian DNG metamaterials by auxiliary differential equation method," *J. Electromagn. Anal. Appl.*, vol. 6, no. 5, p. 106, 2014.

Saptarshi Mukherjee received the B.Tech. degree in electronics and communication engineering from the National Institute of Technology, Durgapur, India, in 2013, and the Ph.D. degree in electrical engineering from Michigan State University, East Lansing, MI, USA, in 2018. He is currently a Post-Doctoral Research Staff Member with the Lawrence Livermore National Laboratory. His current research interests include electromagnetic imaging, microwave sensors, nondestructive evaluation, and biomedical imaging.

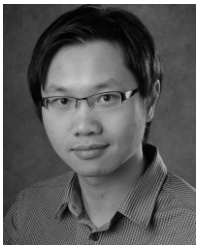

Zhiyi Su (M'18) was born in Guangdong, China, in 1988. He received the B.Eng. and M.Sc. degrees from Tsinghua University, Beijing, in 2011 and 2013, respectively, and the Ph.D. degree from Michigan State University, East Lansing, in 2018. He is currently a Researcher with the Hitachi Automotive Products Research Laboratory (APL), Global Center of Social Innovation—North America. His research interests are electromagnetic computation, advanced material and sensing technology, and design optimization.

Lalita Udpa (F'08) received the Ph.D. degree in electrical engineering from Colorado State University, Fort Collins, CO, USA, in 1986. She is currently a Professor with the Department of Electrical and Computer Engineering, Michigan State University, East Lansing, MI, USA. Her current research interests are in the broad areas of nondestructive evaluation (NDE) and structural health monitoring (SHM) computational electromagnetics, signal processing, and data fusion application for inverse problem solutions in NDE. She is a Fellow of the American Society for Nondestructive Testing and the Indian Society for Nondestructive Testing. She is an Associate Technical Editor of Research Techniques in NDE and an Editor for the IEEE TRANSACTIONS ON MAGNETICS.

Satish Udpa (F'03) received the Ph.D. degree in electrical engineering from Colorado State University. He served as the Dean of the College of Engineering and the Chair of the Electrical and Computer Engineering Department at Michigan State University (MSU) before his current appointment. He serves MSU as the Acting President and the University Distinguished Professor. Prior to joining MSU in 2001, Dr. Udpa was the Whitney Professor of Electrical and Computer Engineering with Iowa State University. He was on the Faculty at Colorado State University prior to his stint at Iowa State University. He has published extensively, holds several patents, and is the Technical Editor of the *Electromagnetic Nondestructive Testing Handbook* (American Society for Nondestructive Testing). His research interests span the broad areas of materials characterization and nondestructive evaluation (NDE). He is a Fellow of the National Academy of Inventors, the American Society for Nondestructive Testing, the Indian Society for Nondestructive Testing, and the Engineering Society of Detroit. He is also a Full Member of the Academia NDT International. He has served as an Editor of the IEEE TRANSACTIONS ON MAGNETICS. He is the Regional Editor of the *International Journal of Applied Electromagnetics and Mechanics*. He also served as the Permanent Secretary of the World Federation of NDE Centers from 1998 to 2003.

Antonello Tamburrino (M'97–SM'18) received the Laurea degree *(summa cum laude)* in electronic engineering from the University of Naples Federico II, Naples, Italy, in 1992, and the Ph.D. degree in electronic engineering from the Polytechnic of Turin, Turin, Italy, in 1996. Since 2006, he has been a Full Professor of Electrical Engineering with the Department of Electrical and Information Engineering, University of Cassino and Southern Lazio, Cassino, Italy. From 2014 to 2018, he was a Full Professor of Electrical Engineering with the College of Engineering, Michigan State University, East Lansing, MI, USA. He has authored or co-authored more than 240 papers that have appeared in refereed international journals, books, and proceedings of international conferences. He is a co-editor of three proceedings. His current research interests include computational electromagnetism, plasmonics, homogenization methods, inverse problems, electromagnetic imaging, and nondestructive evaluation of structures and materials. He is a member of the Scientific Board of the journal *Nondestructive Testing*. Dr. Tamburrino is currently the Subject Editor of the scientific journal *NDT & E International*.